Experimental Mechanics (2012) 52:951–963
DOI 10.1007/s11340-011-9555-3

Out-of-plane Testing Procedure for Inverse Identification Purpose: Application in Sheet Metal Plasticity

T. Pottier · P. Vacher · F. Toussaint · H. Louche · T. Coudert

Received: 1 March 2011 / Accepted: 13 September 2011 / Published online: 14 October 2011

Abstract Many recent works in inverse identification of constitutive parameters have pointed to the need of tests which exhibit heterogeneous strain paths. The present study details a new testing procedure based on out-of-plane motion capture by Stereo-Image Correlation (SIC). With the original test proposed hereby, a unique sample is deformed on a tensile machine along two perpendicular tensile directions, two perpendicular shear directions and one expansion area. The choice of the sample shape is discussed along with the stereo imaging device, 3D reconstruction and measurement uncertainties. The test sample is made from a sheet of commercially pure titanium. A Finite-Element updating inverse method is applied in order to identify six parameters of an anisotropic plastic constitutive model. Results show that this new testing procedure allows every constitutive parameter of the model to be identified from one and only one test.

Keywords Full-field measurement · Heterogeneous tests · Inverse methods · Parameter identification · Stereo image correlation · Plastic constitutive model

T. Pottier (✉)
Chiang Mai University, Faculty of Engineering, Department of Mechanical Engineering, Chiang Mai 50200, Thailand
e-mail: thomas.pottier@univ-savoie.fr

P. Vacher · F. Toussaint
Laboratoire SYMME, Université de Savoie, Polytech'Annecy-Chambéry BP 80439, 74944 Annecy le Vieux Cedex, France

P. Vacher
e-mail: pierre.vacher@univ-savoie.fr

H. Louche
Laboratoire de Mécanique et Génie Civil, Université Montpellier II, pl. E. Bataillon, 34095 Montpellier Cedex, France

T. Coudert
SINTEF Materials and Chemistry, Trondheim, Norway

Introduction

Within the last two decades, numerical mechanics through the Finite Element analysis has been widely used to predict structural behavior. Nevertheless, the wide applicability of the FE approach is responsible for the constant development of new material constitutive models and their increasing complexity. Thus, plenty of models that describes further and further the material behavior have been proposed [1–5].

From an experimental point of view, the parameters identification of such models appears to be time consuming and expensive. Indeed the complexity of the phenomenon taken into account significantly increases the number of parameters to be experimentally identified and implies a multiplication of the required tests.

As a response to such issues, the use of full field measurements coupled with inverse approach has been developed for identification purpose. It aims at retrieving as much parameters as possible from a single heterogeneous test. In many recent studies, the identification of constitutive parameters is done using inverse methods. As pointed in Grediac et al. and Avril et al. [6, 7], the use of such methods often requires (1) overdetermined measured quantities and (2) a sensitivity of these

measured quantities over every constitutive parameter. In practice it appears that classical homogeneous tensile/shear tests are not sufficient to satisfy these two conditions when constitutive models to identify become complex or anisotropic.

Several works have tried to setup heterogeneous tests using uniaxial or bi-axial tensile devices. For example, many authors have presented notched samples undergoing various levels of tensile strains [8–10]. Meanwhile, other studies [11–13] has proposed to add holes to different samples shapes in order to heterogenize the observed tensile strains. A sample geometry that exhibits both shear and tensile behaviors is also proposed in [12]. Finally, various cruciform sample geometries [14–17] operated with bi-axial tensile devices, present heterogeneous strain states namely tension (along two directions) and expansion. However, these studies are based on in-plane sample motion and assume in-plain stress state.

Subsequent works have been performed based on the out-of-plane deformation of the sample. Several testing procedures have been proposed for inverse identification purpose such as three points flexion [18], bulge tests using circular or oblong blanks [19] and a wide range of deep-drawing operations [20, 21].

The present paper proposes a new experimental procedure based on the use of a simple uniaxial tensile device with a sample which leads to an out-of-plane motion. Stereo-Images Correlation [22, 23] is used for motion capture and an inverse identification method is applied to obtained measurements. Firstly, the experimental procedure is presented. Then the numerical model and the investigated constitutive laws are detailed. Finally, the results are discussed and validated.

Experimental Developments

Heterogeneous 3D Test

The proposed experimental procedure is close to the Nakazima test [21]. However, the sample geometry was designed in order to exhibit highly heterogeneous strain paths. Figure 1(a) presents the experimental setup. A hemispherical punch, shown in Fig. 1(b) (diameter ⌀15 mm), is used to apply the prescribed displacement at the sample center. This latter is circular and is tightly encircled and fastened between the die and the holder. Two digital cameras are located above the sample and capture the displacement fields along the x, y and z axis during the deformation process.

In this paper, tests are performed using a Instron 5 kN testing machine. The prescribed displacement speed is set to 5 mm/min.

Sample Design

The diameter of the sample is 100 mm and its thickness is 0.5 mm. The sample has been designed in order to exhibit tension (at 0° and 90° from the rolling direction), shear (at 0° and 90°) and expansion. Samples were manufactured by wire electrical discharge machining. The principal strain directions and magnitudes, plotted as arrows in Fig. 2, shows the sample geometry and the three zones where tension, shear and expansion occurs.

The chosen identification method means that the test has to be modeled in a Finite Element code. However, numerical simulations face the problem of the knowledge of the necking area locations which is not obvious in a classical tensile test. For this purpose, special

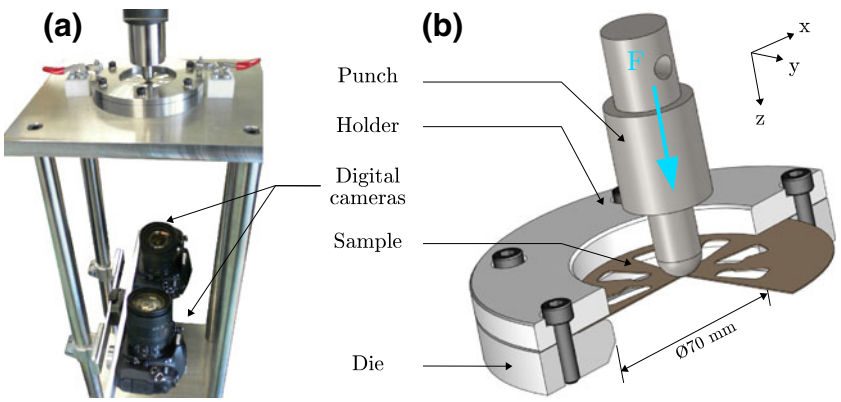

Fig. 1 (**a**) Photograph of the experimental device with stereo imaging cameras. (**b**) Sample and tooling

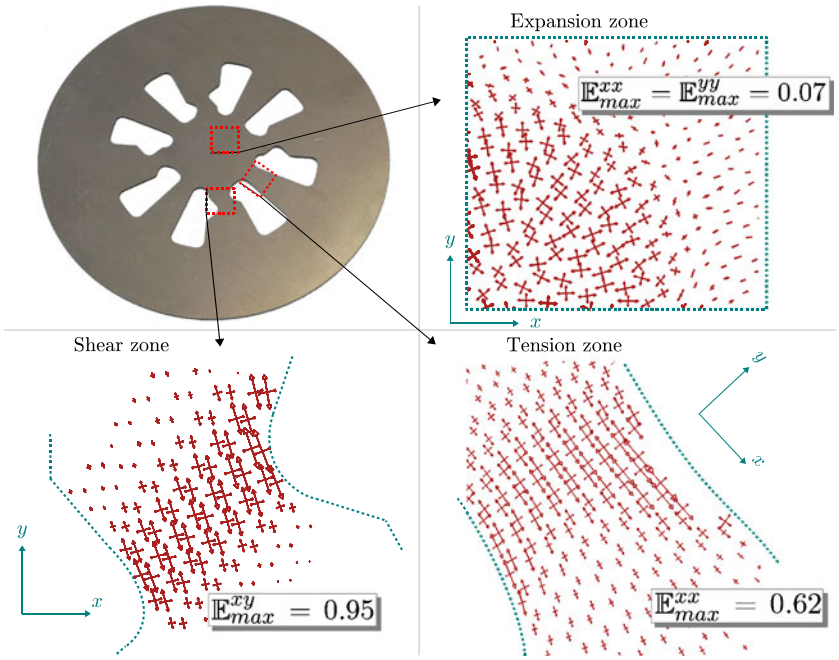

Fig. 2 Sample geometry and principal strain directions after punch displacement $u_z = 10$ mm. $\mathbb{E}$ is the axial component of the Green–Lagrange strain tensor

attention has been paid to the sample design in order to know precisely where necking will occur. Moreover, the sample was numerically designed in order to have an isoprobability of fracture in the tension and the shear zones (for an isotropic material).

Strain level in expansion remains weaker than in the tension or shear zones (Fig. 2). A basic solution to this problem would be to decrease the material thickness in the vicinity of the center. However, such a solution has been dismissed because of the changes in material properties that this machining operation induces over the processed surface (surface condition, hardening, local heating...).

Stereo Image Correlation (SIC)

Stereo Imaging Device

The stereo imaging device is made of two Nikon D200 cameras (Fig. 1(a)) and 3D reconstruction is used to assess the displacement fields over the sample surface. Measurements can be led all over the deformation process and several values of the displacement fields are obtained at different step. The cameras are synchronized and triggered with a remote control and the capture frequency is set to 0.33 Hz. With the chosen focal length the resolution is 0.03 mm/pix and the image resolution is set to 2592×3872 gray level pixels and stored as 8 bit. The diameter of the analysis area is restricted by the holding parts (die) and equals 70 mm. Images are post processed using an in-house developed correlation software named *7D* [24].

Calibration

Since the camera sensors transform a 3D scene into a 2D image, the depth data is lost. However, as shown in Fig. 3, if two cameras are used and if their focal axis are non-collinear, the depth data can be retrieved assuming that the baseline vector between the cameras is known, [23, 25]. Calibration consists of assessing this baseline transformation T_c and also in calculating the intrinsic parameters of the camera (focal distance, coordinates of the projection center and the parameters of the lens distortion). For this purpose several images of a planar target are captured with various orientations. The target (Fig. 3) exhibits an *a priori* known random pattern printed on a planar surface.

Let's consider now a point $P(X, Y, Z)$ on the target. Its coordinates in the camera bases are given by

$$\begin{cases} P_1(x_1, y_1, z_1) = T_L \; P(X, Y, Z), \\ P_2(x_2, y_2, z_2) = T_R \; P(X, Y, Z), \\ P_2(x_2, y_2, z_2) = T_C \; P_1(x_1, y_1, z_1) \\ \qquad\qquad = T_R T_L^{-1} \; P_1(x_1, y_1, z_1), \end{cases} \tag{1}$$

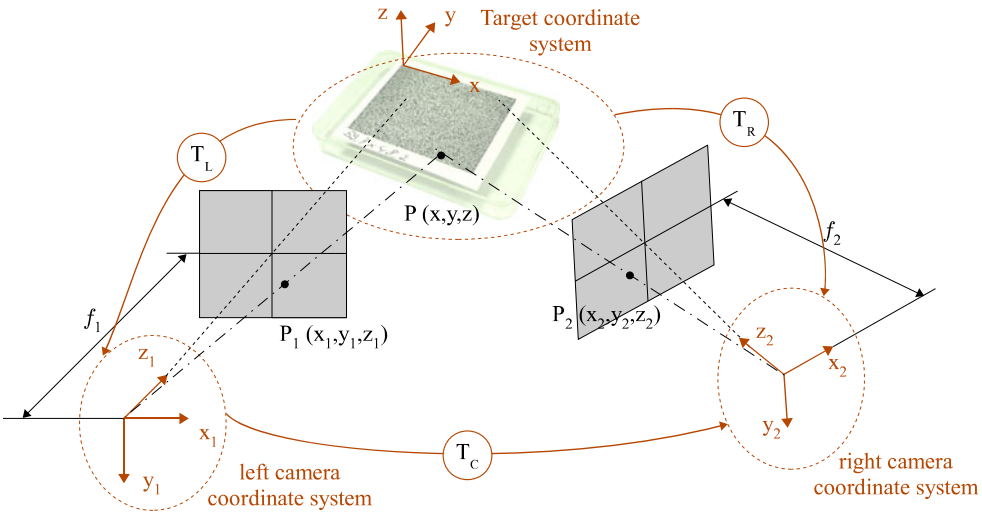

Fig. 3 Geometrical problem of stereo-vision

where T_L and T_R are the transformation from the target base to the left and right camera coordinate systems respectively. Hence, the knowledge of T_C gives the matching of left and right images. However, such a transformation depends on the intrinsic and distortion parameters. In the present study, this problem is solved using a Levenberg–Marquardt [26] optimization algorithm.

Images Matching and Triangulation

Once calibration is completed, the coordinates of P_1 and P_2 can be expressed in the same coordinate system and triangulation can be achieved for any point which appear in both images. Image matching is performed through planar digital image correlation and a gray level speckle is processed over the sample surface. Deformed images (from left and right cameras) are compared to the undeformed left image using *7D* software. The resolution of the extensometric grid and the zone of interest around each point of this grid are both set to 16×16 pixels, corresponding to 0.48×0.48 mm^2. The correlation coefficient is calculated using a *zero-mean normalized cross correlation* formulation. In order to avoid error propagation, each image is correlated with the first left image.

Finally, a non-planar surface is obtained for each pair of images and the displacement fields of each element are then assessed.

3D Measurements Uncertainties

The uncertainties of the SIC measurements are related to miscellaneous factors and are therefore difficult to assess. The numerical acquisition procedure described above exhibits a sensitivity to several parameters [25, 27–30] such as camera noise, lighting, focal distance, magnification, speckle size, strain gradient, *etc.* The measurement error e_{meas} can be classically split in a sum of a systematic error Δ_s and a random error σ_r:

$$e_{\text{meas}} = \Delta_s + \sigma_r. \tag{2}$$

Systematic error

In order to assess the systematic error, a 3D digitization of a Reference Part (RP) is performed (Fig. 4). This digitization is then compared to measurements obtained by a Coordinates Measuring Machine (CMM) which exhibits a ± 1 µm accuracy . As seen in Fig. 4, the RP is made of 6 planes, facing each other two by two.

The distances between the centers of the associated mean square planes and the angles between their normals are estimated and compared in Table 1.

It can be seen in Table 1 that the SIC digitization provides slightly smaller distances between associated planes that the CMM measurement. This may be related to the target measurement (calibration step) that

Table 1 Measured distances and angles between associated planes

Planes	Distance SIC (mm)	Distance CMM (mm)	Difference (µm)	Angle SIC (°)	Angle CMM (°)	Difference (°)
$< a >$ and $< b >$	10.463	10.466	2.70	0.080	0.057	0.023
$< c >$ and $< d >$	17.595	17.617	21.4	0.109	0.097	0.012
$< e >$ and $< f >$	15.995	16.017	21.5	0.190	0.229	−0.039

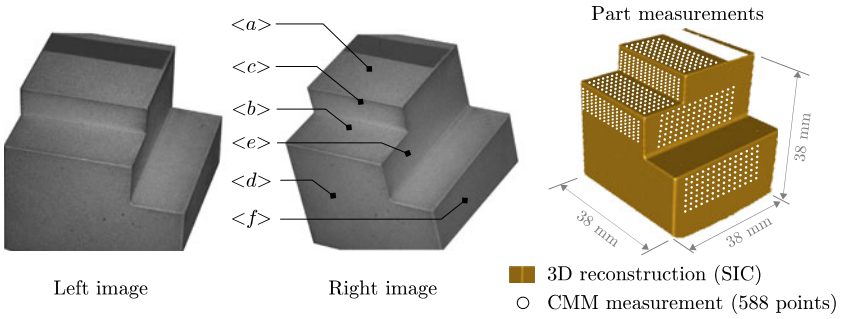

Fig. 4 Measurements of the 6 planes of the reference part by SIC and CMM

is hereby performed using manual caliper. However, further research will address this precise topic. In this paper, such a size magnification is assumed to remain constant during the test and therefore not to affect the assessment of displacements.

Random error

In the present study, the random error is assessed by computing the difference between two digitisations of the RP after a displacement of 9 mm and a rotation of 10°. The capture and post-processing parameters are the same as during the real test. Two pairs of images are successively acquired. The obtained 3D surfaces (6 planes) are then adjusted by a mean-square routine and normal distances are estimated. Figure 5(a) shows the normal distance field and Fig. 5(b) presents their distribution. It can be seen that the random error exhibits a zero-mean normal distribution with a standard deviation of 5 μm. Subsequently, measurement uncertainty is assumed to be a normally distributed random variable such as: $e_{\text{meas}} \sim \mathcal{N}(0\ \mu\text{m}; 5\ \mu\text{m})$.

Furthermore, assuming that, most of the parameters involved remain constant during the tests (lighting, focal distance, magnification, speckle size, pattern size, angle between the cameras, calibration), their systematic error does not affect the measurements. Thus, as described in [31], if the influence of the parameters on the systematic error is dismissed, measurement error can be approximated by the random error. In the present study, this approximated normal distribution is assumed to represent the experimental measurement noise. One must notice that such a procedure does not take into account the influence of strain gradient and part deformation. Therefore, it provide a weak approximation of the measurement error. More detailed assessment of SIC measurement uncertainties are addressed in [23, 32, 33].

Inverse Identification

Material Behavior

In the present study, an anisotropic elastic-plastic behavior is assumed and six parameters are investigated. The elastic behavior is herein defined by an orthotropic model. Previously identified using a standard identification approach [34], the elastic parameters are summarized in Table 2.

Hardening behavior is described using a Ludwick's flow rule such as:

$$\sigma_y^{\text{eq}} = \sigma_y^0 + K(\varepsilon_p^{\text{eq}})^n, \tag{3}$$

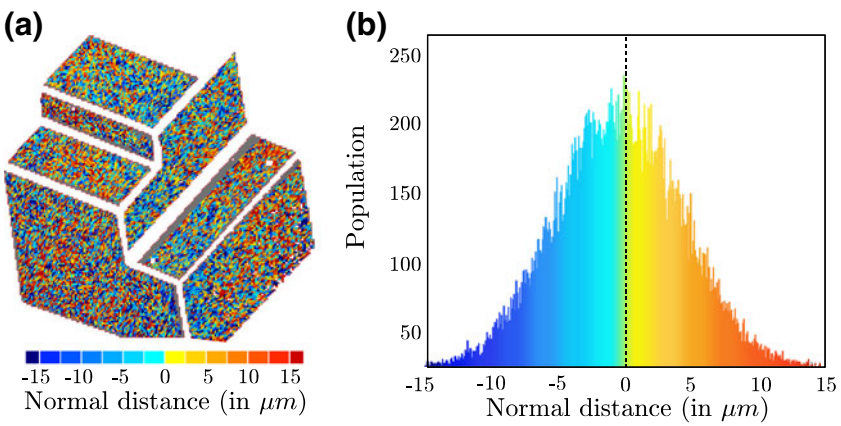

Fig. 5 (**a**) Measured distance field between two digitizations of the reference part (RP) after a displacement of 9 mm and a rotation of 10°. (**b**) Histogram of the measured distances and random error distribution

Table 2 Parameters of the elastic orthotropic model

Parameters	E_x	E_y	ν_{xy}	G_{xy}	σ_y^0
Values	99.5 GPa	111 GPa	0.29	51.7 GPa	368 MPa

where ε_p^{eq} is the equivalent plastic strain, σ_y^{eq} is the current yield stress, σ_y^0 is the initial yield stress. Finally, K and n are two parameters to identify.

Moreover, an orthotropic plastic material behavior is assumed and the Hill 1948 criterion is used [1]. This criterion is commonly used for sheet metal anisotropic behavior including titanium laminates [35]. In the case of plane stress, which is assumed here, the Hill's criterion gives:

$$\mathscr{J}(\sigma) = \sqrt{F\sigma_{22}^2 + G\sigma_{11}^2 + H(\sigma_{11}^2 - \sigma_{22}^2) + 2N\sigma_{12}^2}, \quad (4)$$

where the σ_{ij} are the Cauchy stress tensor components. Therefore, the description of material anisotropy requires four parameters to be identified: F, G, H and N.

Finite Elements Model and Boundary Conditions

Since the identification problem is solved using a Finite Element Update (FEU) inverse method, a numerical model that duplicates the experiment has to be built. The experiment is modeled using Abaqus-Explicit FE code. The sample geometry is meshed using approximatively 18,000 quadrangular solid elements (3 layers through thickness). The punch and the die are considered as analytical rigid bodies. Prescribed displacement at each step is imposed according to the SIC measured displacement at the sample center. Two boundary conditions are applied according to the following considerations:

Punch-blank interaction The friction under the punch is taken into account by a Coulomb's type law. The friction coefficient is set to 0.25 according to former studies performed with the same materials [36]. In order to verify that the chosen value is able to model properly the friction phenomenon, a comparison between experiment and model is done. In practice, the friction induces a localization of the maximum expansion strain on a ring around the sample center (Fig. 6(a)). The diameter and the magnitude of this ring is directly related to the value of the friction coefficient [21, 37]. It can be seen in Fig. 6 that assuming a friction coefficient of 0.25, the strain distributions at the center and on the ring are identical. Therefore, the chosen value of the friction coefficient is assumed to provide a reliable prediction of the stain and displacement fields.

In addition, one should notice that the sample exhibits a central symmetry which ensures the displacements under the punch to remain low.

Die-blank interaction This interaction has been modeled as a fixed boundary condition applied over the sample periphery. However, as can be seen in Fig. 1(b), the contact surface of both die and holder with the sample are flat. Therefore it must be verified that no slipping of the sample occurs. For this purpose, radial displacement has been measured all along the sample diameter at the end of the deformation process. An extrapolation of this measurements has been computed in order to verify that the displacement is zero at the die-blank contact location.

As it can be seen in Fig. 7, the radial displacement of the sample on the inner diameter of the die equals zero. Subsequently, the manual torque applied to the six screws is assumed to ensure that no slipping occurs between the sample and the holding parts.

Identification Strategy

As presented in Fig. 8, the surface displacement fields along x, y and z axis and the global reaction force F are retrieved from the FE simulation and compared to the experimental ones in order to build a mean-square

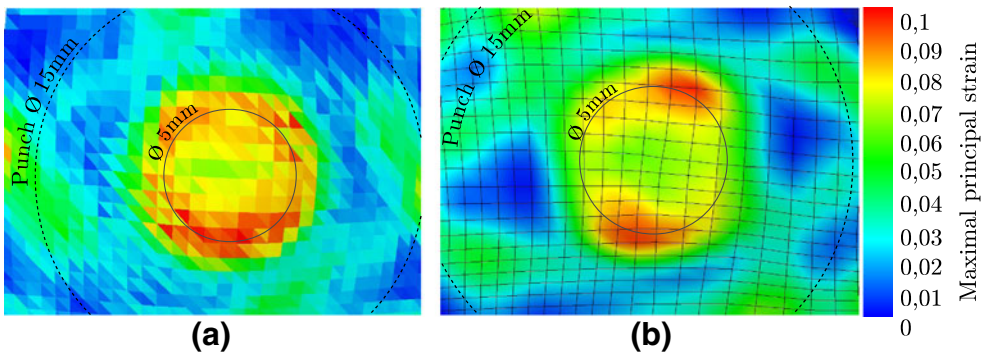

Fig. 6 (**a**) Principal strain measurement at the end of the test highlighting the localization ring of the maximal principal strain. (**b**) Model prediction using finite element analysis at the same instant of the deformation process ($f = 0.25$)

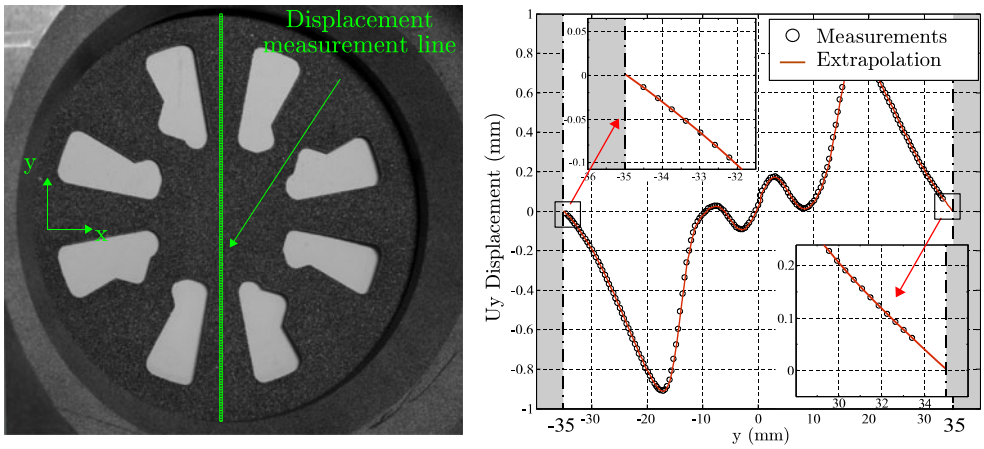

Fig. 7 The measurement of radial displacement over the sample allows to verify that no slipping occurs between the blank and the holding parts (punch displacement $u_z = 10$ mm)

cost-function [38]. Parameter update is performed with a Levenberg–Marquardt optimization algorithm that minimizes the residual gap between experimental and numerical calculations [26].

As proposed for instance in [12, 18, 39] and many others, displacement fields are chosen as field output of the problem. Besides, the comparison of force data is also taken into account. Finally, output data are normalized in order to process dimensionless quantities. Therefore, the cost-function can be written as:

$$f(p) = \left[\sum_{i,j=1}^{N_t,N_r} \left(\frac{u_{x,ij}^{\mathrm{EF}}(p) - u_{x,ij}^{\mathrm{exp}}}{\max\limits_{i,j}(u_x^{\mathrm{exp}})} \right)^2 + \left(\frac{u_{y,ij}^{\mathrm{EF}}(p) - u_{y,ij}^{\mathrm{exp}}}{\max\limits_{i,j}(u_y^{\mathrm{exp}})} \right)^2 + \left(\frac{u_{z,ij}^{\mathrm{EF}}(p) - u_{z,ij}^{\mathrm{exp}}}{\max\limits_{i,j}(u_z^{\mathrm{exp}})} \right)^2 + N_r \left(\frac{F_i^{\mathrm{EF}}(p) - F_i^{\mathrm{exp}}}{\max\limits_{i}(F^{\mathrm{exp}})} \right)^2 \right]^{\frac{1}{2}}, \tag{5}$$

where N_r is the number of material responses and N_t the number of time steps considered, p is the parameter vector.

Mapping of Experimental and Numerical Data

Since the assessment of the cost function requires the experimental and the numerical displacement fields to be compared at the same location, data must be expressed in the same coordinate system. For this purpose, a three-step mapping procedure that evaluates the six components of the related rigid transformation (r_x, r_y, r_z and t_x, t_y, t_z), has been developed. This geometrical operation transforms displacement from the experimental coordinate system (x_e, y_e, z_e) to the numerical coordinate system (x, y, z) which is set on the sample geometry (Fig. 9).

– **First step:** a mean square plane P, is fit to the outer periphery of the measured grid. This plane is assumed to be the plane (x, y) of the sample coordinate system and allows the estimation of r_x,

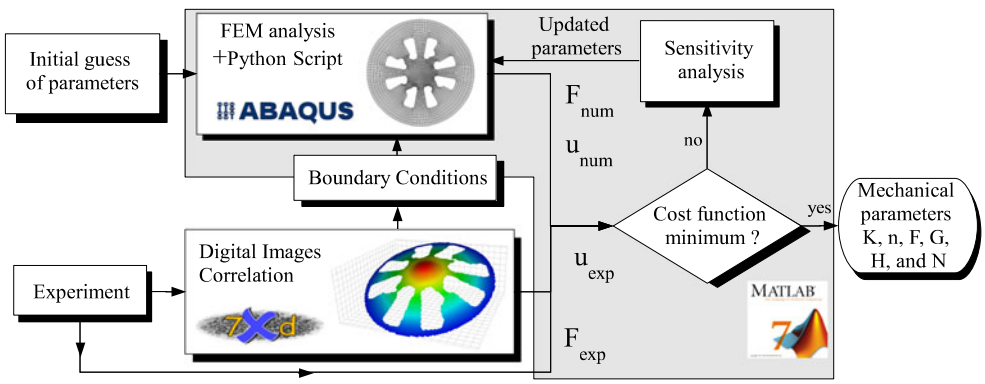

Fig. 8 Iterative solving flowchart of the inverse problem

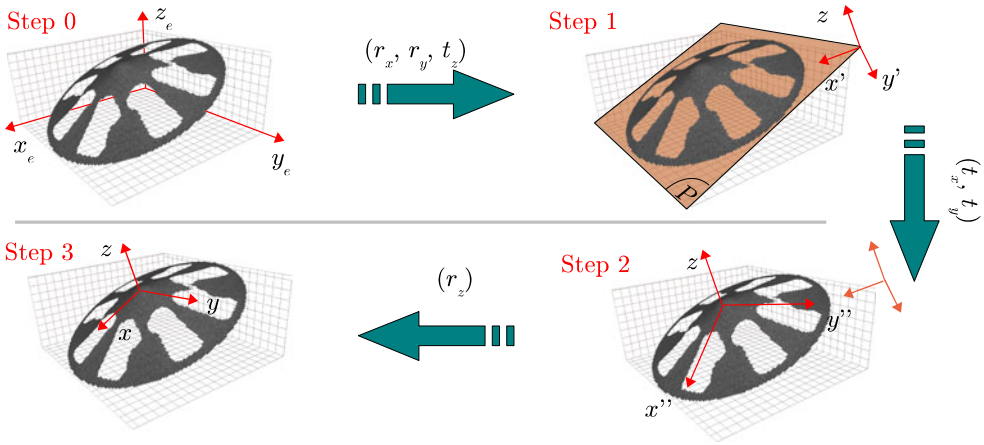

Fig. 9 Three steps procedure developed for data mapping

r_y and t_z. The angular error has been estimated to remain under $e_1 = 0.025°$ [38].

- **Second step:** the center of the sample is localized in both experimental and numerical coordinate systems. The two planar translations t_x, t_y are then assessed within $e_2 = \pm 1/\sqrt{2}$ pixel accuracy [12].
- **Third step:** the planar rotation r_z is evaluated from the given coordinates of a geometrical singularity (corner) in both systems. The assessment also exhibits a $\pm 1/\sqrt{2}$ pixel accuracy at the chosen geometrical singularity. Note that the value of $e_3(r)$ may increase or decrease depending on the radius.

However, an expression in pixel of the mapping error is not relevant if it is not related to the observed displacement gradients. Actually it is noticed that such an error has no effect on constant fields and a major influence on highly heterogeneous fields. Therefore, the three identified errors (in pixel) are added and multiplied by the displacement gradient in order to assess the metric mapping uncertainties along each displacement fields u_x, u_y and u_z. Figure 10 shows the maximum errors fields in µm. Displacement gradient fields are evaluated for a punch displacement of 12.2 mm.

Results and Discussion

Inverse Identification of Plastic Model

The initial set of Hill's parameters are arbitrarily chosen to fit the isotropic case and K and n are chosen according to their known orders of magnitude. For the sake of calculation time, only six time steps of the deformation are considered ($N_t = 6$). The stop criterion is set to end the iterative process if the greatest update value is inferior to 1% of the previous parameter value. In other words, convergence is reached at step k if:

$$\left(p^{(k-1)} - p^{(k)}\right) < p^{(k-1)} \times 0.01. \tag{6}$$

Finally, six parameters of an anisotropic plastic constitutive model are simultaneously identified. Convergence is reached after 11 steps of the updating process. Results are summarized in Table 3.

Figure 11(a) presents the measured and calculated reaction force of the punch versus displacement for the initial parameter set (arbitrarily chosen) and the identified set. Figure 11(b–c) shows the displacement fields along x, y and z measured and calculated with

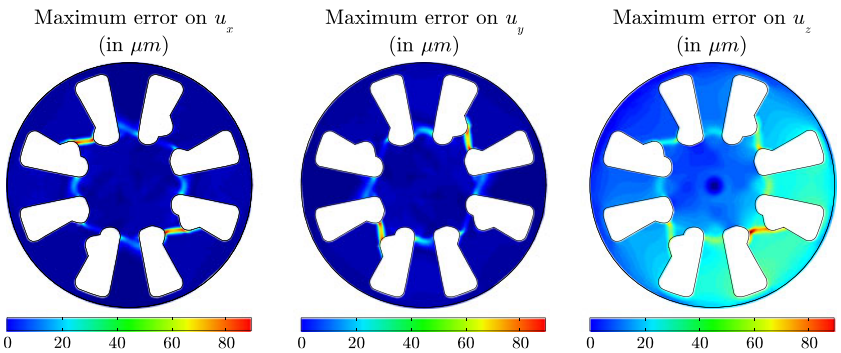

Fig. 10 Fields of maximum mapping error in µm. Gradients of displacement fields are evaluated for a punch displacement of 12.2 mm

Table 3 Identified plastic parameters

Parameters	K	n	F	G	H	N
Initial values	550	0.5	0.5	0.5	0.5	1.5
Identified values	348	0.39	0.31	0.18	0.82	1.9

the identified parameter set. The residual difference between these fields are depicted in Fig. 11(d). It is observed that the identification procedure leads to a good fit between the experimental and numerical reaction forces. A good match of the calculated and the measured displacement field along z is acheived as well.

In addition, it can be seen in Fig. 11(d) that residual displacement fields exhibit significant relative error on u_x and u_y. The magnitude of these residual errors is related to the sum of mapping error, measurement uncertainties, constitutive models approximation, FE modelling, *etc*. It is also noticed that the mapping error is responsible for about 40% of the residual error at high gradient locations (Fig. 10).

Validation: Sensitivity Analysis

Since the parameter set is identified, a first validation can be performed regarding the stability of the iterative procedure. As pointed in many former studies [10, 11, 15, 16, 40–43], investigating the noise sensitivity of the inverse identification procedure allows us to estimate the stability of the minimum reached by the optimization method. In other words, if the obtained parameter set is dependent only on the measurement noise and not on the material behavior itself, identifications using over-noised data will lead to divergent calculated material behavior. In practice, the noise of

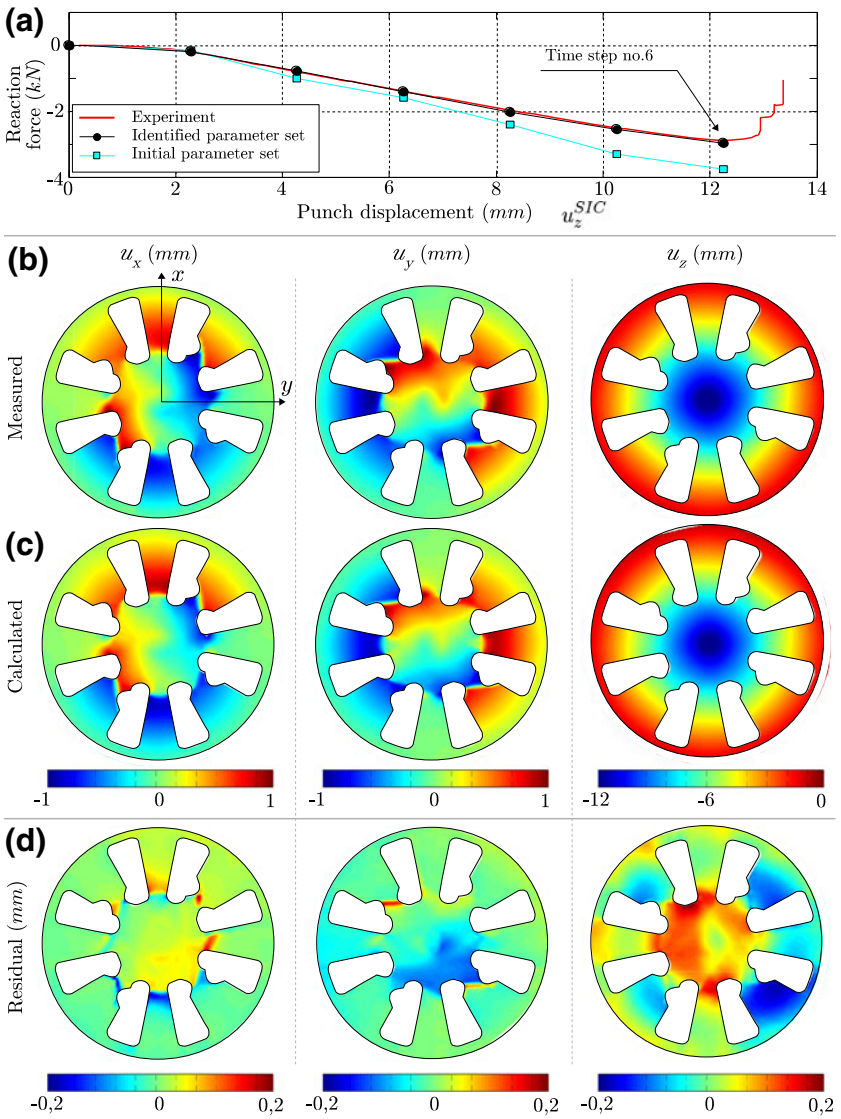

Fig. 11 (**a**) Global punch reaction force before and after identification. (**b**) Experimental measurement of u_x, u_y, u_z displacement fields. (**c**) Predicted u_x, u_y, u_z displacement fields after identification of the material model. (**d**) Residual error after identification on u_x, u_y, u_z displacement fields

Table 4 Parameter sets identified from over-noised data

Parameter	K	n	F	G	H	N	f_{fin}[a]
Reference value	348	0.39	0.31	0.18	0.8	1.9	1.09
Noised value	323	0.44	0.31	0.14	0.86	1.8	1.09
Relative difference (%)	7.2	10	0	22	7.5	5.3	0

[a]Final value of the cost function

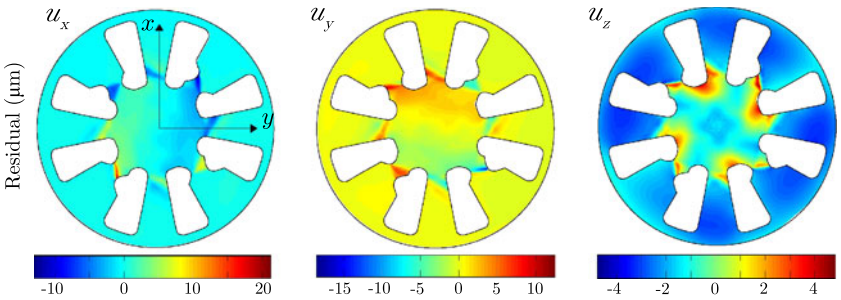

Fig. 12 Residual displacement fields between u^{exp} and $\tilde{u}^{\text{exp}}$

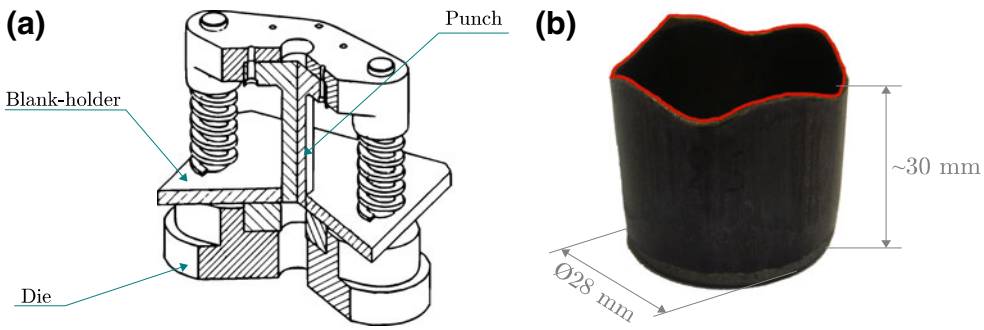

Fig. 13 (**a**) Deep-drawing device. (**b**) Experimental cup shape

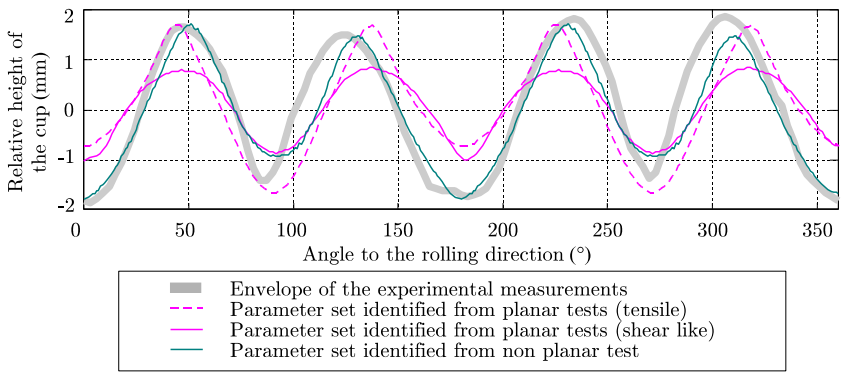

Fig. 14 Comparison of predicted anisotropic profiles

the measuring tools may be responsible for the high deviation of the obtained results. As said above the accuracy of the SIC method is limited and to assess the measurement uncertainties is a tough task. In the present study, the experimental data have been over-noised according to the uncertainty approximation performed above. Thus, random variables are added to the measured displacement fields such as:

$$\begin{cases} \tilde{u}_x^{\exp} = u_x^{\exp} + e_{\text{meas}}/\sqrt{3}, \\ \tilde{u}_y^{\exp} = u_y^{\exp} + e_{\text{meas}}/\sqrt{3} \\ \tilde{u}_z^{\exp} = u_z^{\exp} + e_{\text{meas}}/\sqrt{3}. \end{cases} \quad \text{with } e_{\text{meas}} \sim \mathcal{N}(0\ \mu\text{m};\ 5\ \mu\text{m}), \tag{7}$$

Then, the identification procedure is run again which leads to a new parameter set. The results of this identification are presented in Table 4.

Significant drift of the parameter values is observed in Table 4. However, since the six chosen parameters are not fully independent, a shift of their values may not be relevant of a massive change in the prediction of the whole model. Therefore, the displacement fields predicted by the noised and the noiseless parameter set are compared at the 6th time step (Fig. 12). Despite significant drift of the parameters values (Table 4), the prediction error remains low and below 2%. However, such an error may locally represent up to 10% of the identification residuals on u_x and u_y (Fig. 11).

Finally, even though the noise influence on the identified parameters is obvious, the ability of the model to predict the material behavior appears to be globally unaffected by the assumed measurement noise. In other words, the convexity of the cost function is poor due to dependence of the parameters among them but the number of experimental responses (number of measured points over the sample surface) ensures an acceptable convergence of the optimization algorithm.

Validation: Comparison with a Deep Drawing Test

In order to check the quality of the identified parameter set, validation tests are carried out. The identified parameter set is used to simulate a deep-drawing operation and results are compared to experimental measurements.

On one hand, a deep-drawing device (Fig. 13(a)) is used to obtain 3 experimental cup shapes. The elastic strength of both springs is known and the device is operated using the same tensile machine as described above. Three circular blanks (diameter 60 mm) are formed while the operating force is recorded. The shapes of the three obtained cups are then measured. As shown in Fig. 13(b) the upper profile of the cups exhibits anisotropic horns and their magnitude and frequency are investigated and measured. A Coordinate Measuring Machine (CMM) is used to measure the height of 120 points evenly spread along the upper periphery.

Next, a FE model is developed in order to simulate the experimental deep drawing process. Solid elements are used to model the blank while die, blank-holder and punch are considered as analytical rigid surfaces. The applied load on the blank-holder is picked from the experimental measurements. The friction coefficient is set to $f = 0.25$ in agreement with former results [36]. Furthermore, it has been checked that this parameter does not influence horns anisotropy profiles in a range of $0.1 < f < 0.3$. The upper profile of the cup is then compared to the experimental measurement (Fig. 14) and also compared with a parameter set identified from planar tensile and shear-like tests in [44] using the same material. The parameter set identified from tensile tests is obtained using standard identification method based on specimens cut along 3 different directions.

It can be seen in Fig. 14 that the shape prediction obtained based on non planar test is better than with the planar test. These results are in agreement with previous studies (such as [7, 44]): the increase of the strain field heterogeneity leads to a better assessment of the material behavior through constitutive parameter sets.

Conclusions

In the present paper, an heterogeneous testing procedure, based on out-of-plane deformations and stereo image correlation is presented and applied to parameters identification of material constitutive models. The sample geometry has been designed in order to increase the strain heterogeneities and to exhibit tensile, shear and expansion behaviors. Then, a Finite Element Updating inverse method is used to identify the parameters of an elastic-plastic constitutive model. Results show that a single test can lead the identification of a complete anisotropic plastic model. A study of the mapping error distribution has shown its responsibility for a significant part of the observed residual fields. Noise sensitivity has been investigated and the influence of measurement random error on the obtained results has been discarded. Validation test compare the obtained results with the parameters set assessed by the mean of planar inverse identification on the same material. Results show that identification based on heterogeneous tests lead to better material behavior retrievals. Further study will focus on the extension of the pre-

sented procedure to the identification of more complex plastic models and also elastic and thermal models.

References

1. Hill R (1948) A theory of the yielding and plastic flow of anisotropic metals. Proc R Soc Lond, A 193:281–297
2. Ferron G, Makkouk R, Morreale J (1994) A parametric description of orthotropic plasticity in metal sheets. Int J Plast 10(5):431–449
3. Barlat F, Becker RC, Hayashida Y, Maeda Y, Yanagawa M, Chung K, Brem JC, Lege DJ, Matsui K, Murtha SJ, Hattori S (1997) Yielding description for solution stenghtened aluminum alloys. Int J Plast 13:385–401
4. Cazacu O, Barlat F (2003) Application of the theory of representation to describe yielding of anisotropic aluminum alloys. Int J Eng Sci 41(12):1367–1385
5. Hu W (2007) A novel quadratic yield model to describe the feature of multi-yield-surface of rolled sheet metals. Int J Plast 23:2004–2028
6. Grédiac M (2004) The use of full-field measurement methods in composite material characterization: interest and limitations. Compos, Part A Appl Sci Manuf 35:751–761
7. Avril S, Bonnet M, Bretelle AS, Grédiac M, Hild F, Ienny P, Latourte F, Lemosse D, Pagano S, Pagnacco E, Pierron F (2008) Overview of identification methods of mechanical parameters based on full-field measurements. Exp Mech 48:381–402
8. Kajberg J, Lindkvist G (2004) Characterization of materials subjected to large strains by inverse modeling based on in-plane displacement fields. Int J Solids Struct 41:3439–3459
9. Pannier Y (2006) Identification de paramètres élastoplastiques par des essais statiquement indéterminés : mise en œuvre expérimentale et validation de la méthode des champs virtuels. PhD thesis, Ecole National Supérieure des Arts et Métiers, France
10. Belhabib S, Haddadi H, Gaspérini M, Vacher P (2007) Heterogeneous tensile test on elastoplastic metallic sheets: comparison between FEM simulations and full-field strain measurements. Int J Mech Sci 50:14–21
11. Molimard J, Le Riche R, Vautrin A, Lee JR (2005) Identification of the four orthotropic plate stiffnesses using a single open-hole tensile test. Exp Mech 45:404–411
12. Meuwissen MHH (1998) An inverse method for mechanical characterization of metal. PhD thesis, Eindhoven University of Technology, Netherlands
13. Cooreman S (2008) Identification of the plastic material behaviour through full-field displacement measurements and inverse methods. PhD thesis, Vrije Universitet Brussel, Belgique
14. Kuwabara T, Kuroda M, Tvergaard V, Nomura K (2000) Use of abrupt strain path change for determining subsequent yield surface: experimental study with metal sheets. Acta Mater 48:2071–2079
15. Lecompte D, Smits A, Sol H, Vantomme J, Van Hemelrijck D (2007) Mixed numerical-experimental technique for orthotropic parameter identification using biaxial tensile test on cruciform specimens. Int J Solids Struct 44:1643–1656
16. Promma N, Raka B, Grédiac M, Toussaint E, LeCam J-B, Balandraud X, Hild F, Application of the virtual fields method to mechanical (2009) characterization of elastomeric materials. Int J Solids Struct 46:698–715
17. Guélon T, Toussaint E, Le Cam J-B, Promma N, Grédiac M (2009) A new characterisation method for rubber. Polym Test 28(7):715–723
18. Bruno L, Felice G, Pagnotta L, Poggialini A, Stigliano G (2008) Elastic characterization of orthotropic plates of any shape via static testing. Int J Solids Struct 45:908–920
19. Chamekh A, BelHadjSalah H, Hambli R, Gahbiche A (2006) Inverse identification using the bulge test and artificial neural networks. J Mater Process T echnol 177(1–3):307–310
20. Ghouati O, Gelin JC (2001) A finite element-based identification method for complex metallic material behaviours. Comput Mater Sci 21:57–68
21. Forestier R (2004) Développement d'une méthode d'identifcation de paramètres matériaux par analyse inverse couplée avec un modèle éléments-finis 3D. PhD thesis, Ecole Nationale Supérieure des Mines de Paris
22. Garcia D, Orteu JJ, Penazzi L (2002) A combined temporal tracking and stereo-correlation technique for accurate measurement of 3D displacements: application to sheet metal forming. J Mater Process Technol 125–126:736–742
23. Coudert T (2005) Reconstruction tridimensionnelle du volume intérieur d'une chaussure: évaluation du chaussant. PhD thesis, Université de Savoie
24. Vacher P, Dumoulin S, Morestin F, Mguil-Touchal S (1999) Bidimensional strain measurement using digital images. Proc Inst Mech Eng 213:811–817
25. Sutton MA, Yan JH, Tiwari V, Schreier WH, Orteu JJ (2008) The effect of out-of-plane motion on 2D and 3D digital image correlation measurements. Opt Lasers Eng 46:746–757
26. Marquardt DW (1963) An algorithm for least-squares estimation of nonlinear parameters. J Soc Ind Appl Math 11:431–441
27. De Almeida O, Lagattu F, Brillaud J (2008) Analysis by a 3D DIC technique of volumetric deformation gradients: application to polypropylene/EPR/talc composites. Compos, Part A 39:1210–1217
28. Haddadi H, Belhabib S (2008) Use of rigid-body motion for the investigation and estimation of the measurement errors related to digital image correlation technique. Opt Lasers Eng 46:185–196
29. Pan B, Xie H, Gao J, Asundi A (2008) Improved speckle projection profilometry for out-of-plane shape measurement. Appl Opt 47:5527–5533
30. Pan B, Lu Z, Xie H (2010) Mean intensity gradient: an effective global parameter for quality assessment of the speckle patterns used in digital image correlation. Opt Lasers Eng 48:469–477
31. Chambard J-P, Jaminion S, Tazeroualti M, Galerne C, Hild F (2009) 3D displacement field measurement by digital image correlation - metrological study and application to composite structures. In: Comptes Rendus des JNC 16 – Toulouse
32. Garcia D (2001) Mesure de formes et de champs de déplacements tridimensionnels par stéréo-corrélation d'images. PhD thesis, Institut National Polytechnique de Toulouse
33. Fazzini M (2009) Développement de méthodes d'intégration des mesures de champs. PhD thesis, Université de Toulouse, France
34. Toussaint F, Tabourot L, Ducher F (2008) Experimental and numerical analysis of the forming process of CP titanium scoliotic instrumentation. J Mater Process Technol 197:10–16
35. Haddadi H, Bouvier S, Banu M, Maier C, Teodosiu C (2006) Towards an accurate description of the anisotropic behaviour

of sheet metals under large plastic deformations: modelling, numerical analysis and identification. Int J Plast 22:2226–2271
36. Le Port A, Toussaint F, Arrieux R (2009) Finite element study and sensitivity analysis of the deep-drawing formability of commercially pure titanium. Int J Mater Form 2: 121–129
37. Boissière R (2008) Effet de la température sur les capacités de mise en forme d'alliages de magnésium corroyés. PhD thesis, INP Grenoble, Université de Savoie, France
38. Pottier T (2010) Identification paramétrique par recalage de modèles éléments finis couplée à des mesures de champs cinématiques et thermiques. PhD thesis, Université de Savoie, France
39. Kleinermann J-P (2000) Identification paramétrique et optimisation des procédés de mise en forme par problème inverse. PhD thesis, Université de Liège, Belgique
40. Gelin JC, Ghouati O, Paquier P (1998) Modelling and control of hydroforming processes for flanges forming. Ann CIRP 47(1):213–216
41. Harth T, Schwan S, Lehn J, Kollmann FG (2004) Identification of material parameters for inelastic constitutive models: statistical analysis and design of experiments. Int J Plast 20:1403–1440
42. Amiot F, Hild F, Roger J-P (2007) Identification of elastic property and loading fields from full-field displacement measurements. Int J Solids Struct 44:2863–2887
43. Nakamura T, Liu Y (2007) Determination of nonlinear properties of thermal sprayed ceramic coatings via inverse analysis. Int J Solids Struct 44:1990–2009
44. Pottier T, Toussaint F, Vacher P (2011) Contribution of heterogeneous strain field measurements and boundary conditions modelling in inverse identification of material parameters. Eur J Mech A/Solids 30:372–382